

Geant4 simulation of fast electron bremsstrahlung imaging at the HL-3 tokamak*

Shi-Kui Cheng,^{1,2} Yi-Po Zhang,^{3,†} Yue-Jiang Shi,^{4,5} Jie Zhang,³ Shuai Guan,³ Hong-Bing Xu,³ and Qiu-Lei Yang³

¹College of Science, Chongqing University of Technology, Chongqing, 400054, China

²Chongqing Key Laboratory of New Energy Storage Materials and Devices, Chongqing, 400054, China

³Southwestern Institute of Physics, Chengdu, 610041, China

⁴Hebei Key Laboratory of Compact Fusion, Langfang 065001, China

⁵ENN Science and Technology Development Co., Ltd., Langfang, 065001, China

To further research on high-parameter plasma, we plan to develop a two-dimensional hard X-ray (HXR) imaging system at the HL-3 tokamak to measure HXRs with energies ranging from 20 to 300 keV. The application of an array-structured detector ensures that this system can measure HXR-radiation spectra from the entire plasma cross section. Therefore, it is suitable for the study of fast-electron physics, such as radio-frequency wave current drives, fast electrons driving instabilities, and plasma disruptions in fusion research. In this study, we develop a simulation for calculating fast-electron bremsstrahlung in the HL-3 tokamak based on the Monte Carlo simulation code Geant4, in which the plasma geometry and forward scattering of fast-electron bremsstrahlung are considered. The preliminary calculation results indicate that the HXR energy deposition on the detector is symmetrically distributed, even though the plasma distribution is asymmetric owing to the toroidal effect. These simulation results are helpful in constructing the relationship between the energy deposition on the detector and parameter distribution on the plasma cross section during HL-3 experiments. This is beneficial for the reconstruction of the fast-electron distribution function and for optimizing the design of the HXR-imaging system.

Keywords: Geant4 simulation, HL-3 tokamak, Fast-electron bremsstrahlung, Hard X-ray imaging

I. INTRODUCTION

In tokamak plasma, fast electrons can be produced in many ways, such as through the application of auxiliary heating methods, disruptive events, and sawtooth activities. Although their density is two orders of magnitude below the plasma density, fast electrons play an important role in maintaining the steady operation of tokamaks with high parameters [1, 2]. During radio-frequency (RF) wave heating and current-driven experiments, electrons gain energy from the RF waves through resonance effects and then become fast electrons. The redistribution of fast electrons and their collisions with other plasma ions and electrons eventually increase the plasma temperature and current. However, owing to their low Coulomb-collision resistance, they can be converted into runaway electrons, which form a runaway beam. Once the runaway beam is formed, it may affect the normal operation of the experiments, causing melt damage to the plasma-facing components and divertors [3–7]. In more serious cases, it terminates the discharges and compromises the safe operation of the device. Hard X-rays (HXRs) are produced from collisions between fast electrons and bulk plasma ions and provide a considerable amount of information about fast electrons. Therefore, the measurement of HXRs during plasma discharge is an important method for studying fast-electron physics, such as the build-up of the electron-distribution function, electron cyclotron wave-power deposition profile [1, 2], and dynamics of the instabilities [8, 9].

Most traditional HXR diagnostics depend on arrays of detectors at different toroidal and poloidal locations around the tokamaks, such as HT-6B [10], HT-7 [11, 12], EAST [13], HL-1M [14], HL-2A [15, 16], and EXL-50 [17]. Multidirectional detection has enabled the reconstruction of emission profiles from the plasma cross section [8]. In the TCV tokamak, a multichannel HXR spectroscopy system allows observation of the evolution of the electron distribution related to fishbone oscillations [18]. In the WEST tokamak, the designed two-dimensional (2D) HXR camera provides spatial, temporal, and energy-resolved measurements of the HXR emission from the full plasma cross section, enabling the investigation of the electron temperature and fast-electron tail-density evolution, as well as the characteristics of tungsten X-rays due to beam-target emission at the edge [19]. In the HL-2A tokamak, measurements from an HXR pinhole camera indicate that the spatial distribution of fast electrons during the lower hybrid current drive (LHCD) has a peaked profile, implying that fast electrons are mainly produced in the plasma core [20, 21]. The spatially distributed HXR detection array at the J-TEXT tokamak showed that most runaway electrons transported to the plasma boundary tend to be lost on the limiters [22]. In other fusion devices, more than two arrays are used for tangentially viewing HXR diagnostics, with the help of tomography algorithms; this method has promising applications for the analysis of MHD instabilities in the T-10 tokamak [23] and current-drive efficiency studies in Tore Supra [24].

Owing to the anisotropic characteristics of bremsstrahlung and irregular shape of plasma, inverting line-integrated measurement data to obtain a 2D emissivity distribution is difficult [25]. Therefore, 2D HXR-imaging diagnostics have been developed to consider space requirements and avoid complex correlation and inversion procedures. In the PBX-M tokamak, a 2D HXR camera was applied to obtain direct

* This work was supported by the National Natural Science Foundation of China (No.12305239), Scientific Research Foundation of Chongqing University of Technology (No.2023ZDZ053), and National Key R&D Program of China (No.2019YFE03010001).

† Corresponding author, zhangyp@swip.ac.cn

measurements of the location of the current-driven electrons, which have been used for current profile-modification experiments [26–28]. Additionally, the HXR camera has the capability to observe bremsstrahlung radiation from fast electrons during LHCD experiments, thereby allowing accurate fast-electron-transport studies [29, 30]. In the DIII-D tokamak, an HXR camera was installed on the outer midplane of the tokamak with 123 detectors, which covered most of the plasma volume [31]. An electron-distribution function with 2D spatial resolution was obtained during runaway-electron experiments, allowing the characterization of the evolution of the RE distribution function during RE growth and dissipation [32–34].

Two-dimensional HXR measurements have been successfully implemented in many tokamak devices; however, owing to the spatial asymmetry of the plasma induced by toroidal effects, associating tangential measurements with information on the plasma cross section is difficult. Computing the 2D distribution function of fast electrons and studying the instability physics related to fast electrons is also challenging. Therefore, tangential 2D HXR imaging systems have not been widely implemented in tokamaks. Under such conditions, we conducted a 2D HXR-imaging simulation study on the HL-3 tokamak to determine the correspondence between the images of the tangential HXR-imaging system and plasma cross-section parameters. The significance of the simulation was evident. First, the simulation results can qualitatively show whether the HXR-imaging system is feasible. Second, the HXR-imaging system can be optimized by the simulation results, such as the placement position and shielding structure. Third, the simulation results can help us analyze the measured experimental results and then inversely deduce the radiative properties and distribution characteristics of the fast electrons. The Geant4 simulation model is based on the plasma geometry of the HL-3 tokamak and HXR imaging system, and a fast-electron forward-scattering model is also considered. The remainder of this paper is organized as follows. Sec. II introduces the HL-3 tokamak and HXR diagnostics. A Geant4 simulation model based on the plasma configuration of the HL-3 tokamak and fast-electron bremsstrahlung model containing forward-scattering effects are presented in Sec. III. The preliminary simulation results are presented in Sec. IV. Sec. V provides potential reasons for the energy deposition that appears on the detector. Finally, the summary and discussion are presented in Sec. VI.

II. HL-3 TOKAMAK AND HARD X-RAY DIAGNOSTIC

A schematic of the HL-3 tokamak is shown in Fig. 1, which shows the main parts of the device and the HXR-imaging system. The transparent purple rings denote plasma, and the yellow cylinders are the sight lines of the detector arrays. The HL-3 tokamak is a medium-sized device with a major radius of $R = 1.78$ m, a minor radius of $a = 0.65$ m, an elongation of $\kappa > 1.8$, and a triangularity of $\delta > 0.5$. The main purpose of this device is to support the operation of future fusion devices by integrating the technological and physical

aspects [35, 36]. The designed toroidal magnetic field is approximately 2.2–3 T, and the maximum plasma current is 3 MA. The heating and current-drive systems can provide a total power of 27 MW. The first plasma was successfully produced in 2020 [37], and currently, the maximum plasma current is higher than 1 MA.

The tangentially viewed HXR-imaging system primarily comprises an LYSO scintillator crystal, a SiPM detector array, and online spectra-processing electronics [38]. The system is located outside the vacuum chamber, and a 1-mm-thick beryllium window is used to protect the vacuum. This system can measure HXRs with energies ranging from 20 keV to 300 keV, with a spatial resolution of several centimeters, a temporal resolution of several tens of microseconds, and an energy resolution of approximately 8 % @ 662 keV. The design of the HXR imaging system is illustrated in Fig. 2, where the LYSO scintillator and SiPM array are located inside the tungsten–copper shield; only photons passing through the small pinhole in front of the shield can enter the detector. When a LYSO crystal is struck by X-ray photons, certain wavelengths of visible or near-visible photons are scintillated. The visible light is detected by the SiPM arrays and converted into electrical-pulse signals, and an analog-to-digital converter then digitizes the electrical-pulse signals and delivers them to the FPGA module. The FPGA module rearranges these digitized signals into a specific format to identify the photon energy and deposition time. Finally, the experimental data containing time and pulse-amplitude information are transferred to a remote-controlled PC. The time evolution of the radiation intensity is obtained from the time evolution of the energy deposition on each detector. The spatial positions corresponding to different detectors can reflect the spatial evolution of the radiation intensity. The energy-spectrum information of a specific period can be used to deduce the temperature and distribution characteristics of fast electrons.

III. INTRODUCTION OF GEANT4 SIMULATION MODEL AND FAST-ELECTRON BREMSSTRAHLUNG MODEL

The primary objective of this study is to model X/γ -ray photon-energy deposition on the detector. Similar work has been performed in the EAST tokamak, which simulates the energy response of a scintillating fiber detector using the Geant4 code [39, 40]. We also performed simulations in previous studies, where fast-electron forward scattering was not considered [41]. Initially, we assumed that the direction of movement of each photon was arbitrary. After testing a large number of particles and a long calculation time, the deposited energies on the detector remained very small and did not exhibit any distributional properties.

We performed a simple analysis to explain these results. Because of the shielded collimation system at the front of the HXR-imaging system, only incident-ray photons entering the collimation pinhole can deposit their energy on the detector. On the sight lines of the imaging system, only particles in the cross section of the plasma that are parallel to the surface of the detector have the greatest probability of interacting with

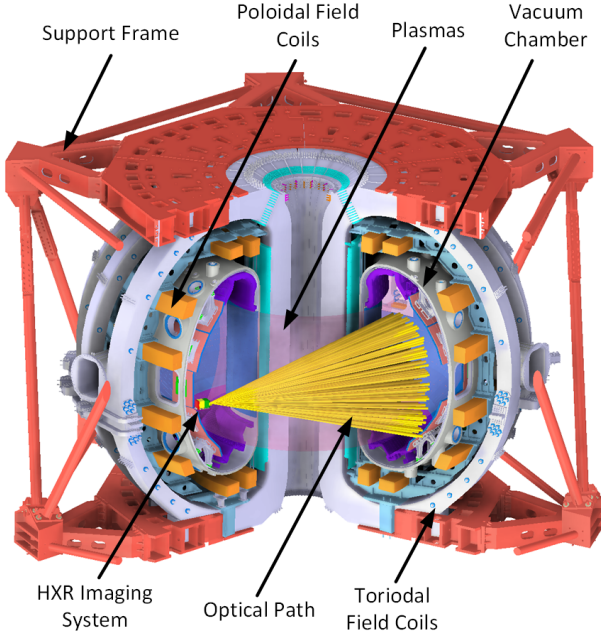


Fig. 1. (Color online) Three-quarter cut-away view of the HL-3 tokamak, where the HXR-imaging system is located between the toroidal-field coil and vacuum chamber. The translucent purple shape is the plasma, and the yellow arrows are the optical path. Other components such as the support frame, vacuum chamber, poloidal field, and toroidal-field coils are also displayed in the figure.

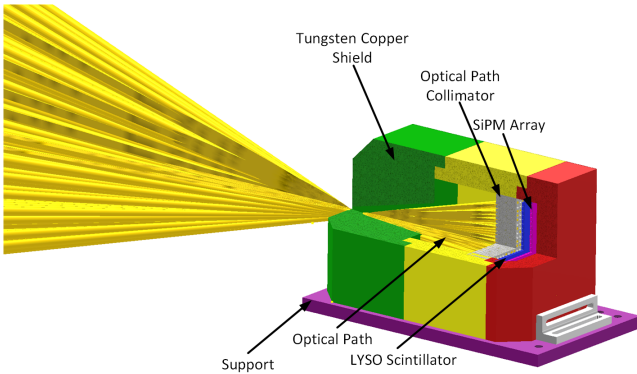


Fig. 2. (Color online) Cut-away view of the HXR system. The LYSO scintillator and SiPM detector are placed inside the shields, and the optical path can cover most of the plasma cross section.

the detector. We use this plane as an example to estimate the value of the maximum probability, where the distance between the collimating pinhole of the HXR-imaging system and plasma cross section parallel to the detector surface is approximately 2.5 m, and the designed collimation pinhole has a diameter of 2 mm. We obtain the following:

$$f_{max} = \frac{\text{Area of the pinhole}}{\text{Area of the radiation sphere}} \quad (1)$$

$$= \frac{\pi \times 0.002^2}{4 \times \pi \times 2.5^2} = 1.6 \times 10^{-7}$$

However, this maximum probability should be divided by a large number (e.g., 50) when considering the entire HL-3 plasma region because the farther the photon is from the plane parallel to f_{max} , the less likely it is to be deposited on the detector. The probability of a photon moving in an arbitrary direction and depositing its energy on the detector is approximately:

$$f_{ave} \approx \frac{f_{max}}{50} = 3.2 \times 10^{-9}. \quad (2)$$

That is, for every 10^{10} X/γ -ray photons, approximately 32 of them will deposit their energy on the detector. To elucidate the energy-deposition distribution, the number of deposited particles would be of the order of one million; thus, the number of X/γ -ray photon sources would be uncountable. This is detrimental to our calculations because this number of particles would be impossible to enter into the Geant4 code; the larger the number of particles, the more resources are consumed by the calculations.

To resolve this problem, we assume that all incident particles move toward the collimation pinhole. Under a particle-source distribution with a slab configuration, the deposited energies on the detector are similar to the distribution of the electron density or temperature on the plasma cross section. Under a particle-source distribution with an HL-3 plasma configuration, the high-field side has more X/γ -ray photons because of the longer chord length, resulting in a deviation of the Gaussian distribution of the energy deposition on the detector. As this model does not match the actual conditions, this part of the calculation deserves further speculation.

In the latest studies, we updated our simulation model based on the HL-3 plasma parameters and forward scattering of fast-electron bremsstrahlung. This section introduces these two models. The first is a fast-electron bremsstrahlung radiation model based on the Geant4 code, where the distribution of X/γ -ray sources refers to the shape of HL-3 plasma, and the X/γ -ray detectors refer to the 2D HXR-imaging system. Other components, such as the stainless-steel vacuum chamber and tungsten copper shields, are also considered in this model. The second is the fast-electron forward-scattering model, in which the HXR emission strongly peaks in the forward direction, and the higher the electron energy, the narrower the emission cones.

The simulation flowchart is shown in Fig. 3. We used an HL-3 tokamak as the particle-source configuration and an HXR-imaging system as the energy-deposition configuration. The particle-source distribution refers to the experimental data from HL-3 discharges, and the particle-motion directions are constructed using a fast-electron forward-scattering model. A sufficiently large number of photons were inputted into Geant4 and the code was run.

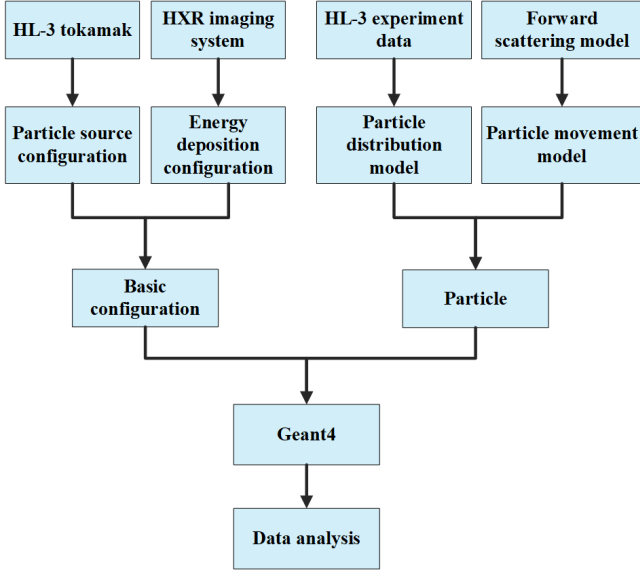


Fig. 3. (Color online) Simulation flow of X-ray photons energy deposition on the detector.

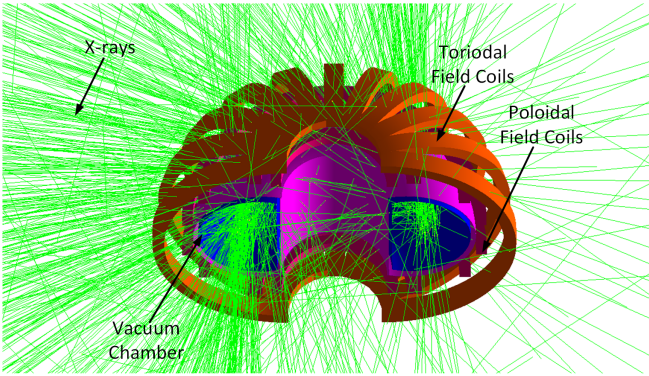


Fig. 4. (Color online) Half-cutaway view of HL-3 device for Geant4 simulation, where the green lines are X-rays, the brown stripes are toroidal and poloidal field coils, and the blue shell is the boundary of HL-3 plasmas.

A. Geant4 Simulation Model

We developed a bremsstrahlung simulation model based on the Geant4 code [42, 43] to simulate energy deposition on the detector. The geometry is defined as a considerably simpler structure than that of a realistic HL-3 tokamak, as shown in Fig. 4, which includes only a copper magnetic-field coil system and stainless vacuum vessel. An LYSO crystal and a single-energy X/γ -ray are used in our simulations. The X/γ -ray source profile is assumed to have a Gaussian distribution in both the radial and vertical directions and has the same dimensions as HL-3 plasma with $R = 1.78$ m, $a = 0.65$ m, and $\kappa = 1.3$. The directions of all the electron motions are parallel to the magnetic axis. Geant4 tracks all X/γ -ray photons until they are absorbed in the materials and records the deposit energy and location when the X/γ -ray photon enters

the LYSO detector.

B. Fast-Electron Bremsstrahlung Model

The simulation is based on the forward scattering of X/γ -ray bremsstrahlung for fast electrons [44], where all electrons are assumed to move from left to right, and each electron emits X/γ -ray photons with energies smaller than their kinetic energies. The calculated results are shown in Fig. 5, where the X/γ -ray emission cones are plotted for electrons with energies of 20, 50, 100, 200, and 500 keV. As shown in this figure, the higher the electron energy, the narrower the bremsstrahlung cones. Therefore, in a tokamak device, if the energetic electrons exhibit speed primarily along the magnetic-field lines, the X/γ -ray emission is strongly peaked in the direction of the toroidal field and opposite to the direction of the plasma current.

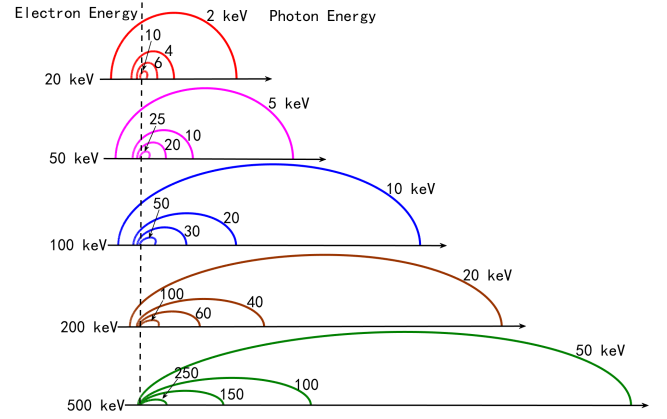


Fig. 5. (Color online) Bremsstrahlung-emission cones for mildly relativistic electrons.

The forward-scattering characteristics are shown more intuitively in Fig. 6. Electrons (yellow dots) moving along the magnetic-field line (red dashed line) emit photons in all directions (green arrows), whereas the photon distribution is the densest (blue dots) in front of the motion. Fig. 7 can be used to describe the entire process: when the electron (red dot) moves to point A along orbit AA' , it has the movement direction of \vec{AB} , the bremsstrahlung intensity is the strongest along \vec{AB} , and the distribution characteristics are $F(u, v, w)$ in all directions.

The first step is to construct a particle-distribution function. By adding three small variables δ_{s1} , δ_{s2} , and δ_{s3} to each coordinate of $A(X_0, Y_0, Z_0)$, we obtain a new point $A_\delta(X_0 + \delta_{s1}, Y_0 + \delta_{s2}, Z_0 + \delta_{s3})$. If δ_{s1} , δ_{s2} , and δ_{s3} take different values and form the set of $\{\{\delta_{s1}\}, \{\delta_{s2}\}, \{\delta_{s3}\}\}$, and they are added to X_0, Y_0, Z_0 respectively, we obtain a point set $\{\{X_0 + \delta_{s1}\}, \{Y_0 + \delta_{s2}\}, \{Z_0 + \delta_{s3}\}\}$, which is centered on (X_0, Y_0, Z_0) , and has a length of $\max(\delta_{s1}) - \min(\delta_{s1})$ in the X direction, width of $\max(\delta_{s2}) - \min(\delta_{s2})$ in the Y direction, and height of $\max(\delta_{s3}) - \min(\delta_{s3})$ in the Z direction. Therefore, the main task in building a particle-distribution model is

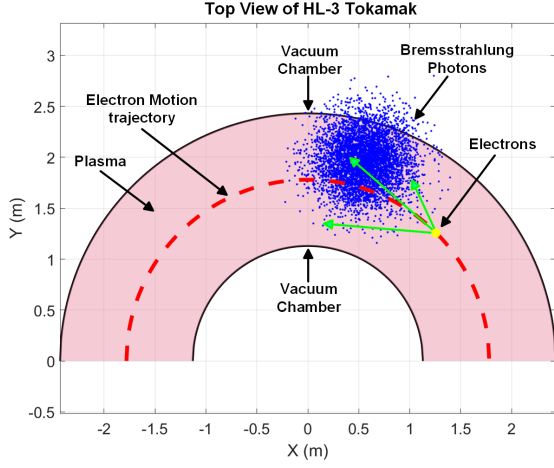


Fig. 6. (Color online) Top view of the fast-electron forward-scattering diagram, where the red shaded area is the HL-3 plasma, the red dashed line is electron motion trajectory, the green arrows are the bremsstrahlung direction, and the blue dots are bremsstrahlung photons.

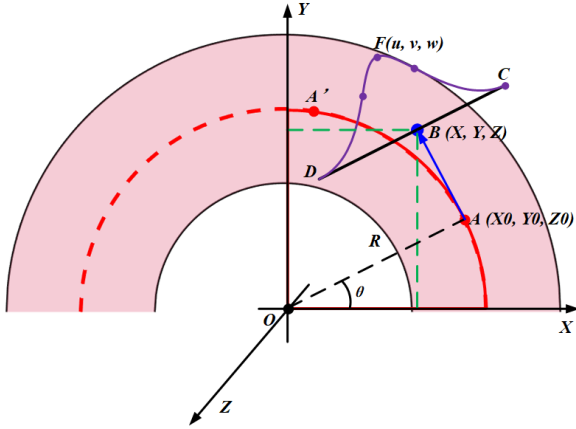


Fig. 7. (Color online) Fast-electron forward-scattering model, where point O is the center of HL-3, R is the minor radius of HL-3, point A is the location of electron, point B is in the movement direction of the electron, $F(u, v, w)$ is the radiation direction function.

to determine suitable values for δ_{s1} , δ_{s2} , and δ_{s3} .

Referring to the HL-3 experiments with RF waves, the electron temperatures and densities approximately obeyed normal distributions in the radial and polar directions (left panel in Fig. 8). Therefore, only a set of random numbers δ_{s1} , δ_{s2} , and δ_{s3} that obey a normal distribution need to be constructed to obtain a distribution model similar to the electron temperature or density profiles (right panel in Fig. 8).

Notably, the direction of electron motion is parallel to the magnetic axis, that is, perpendicular to the cross section where the electrons are located. The electron-motion orbit is on an arc with radius R , such that one set of random numbers with a normal distribution can generate a particle distribution in the X and Y directions. Moreover, because the random distribution of particles in the Z direction is independent of

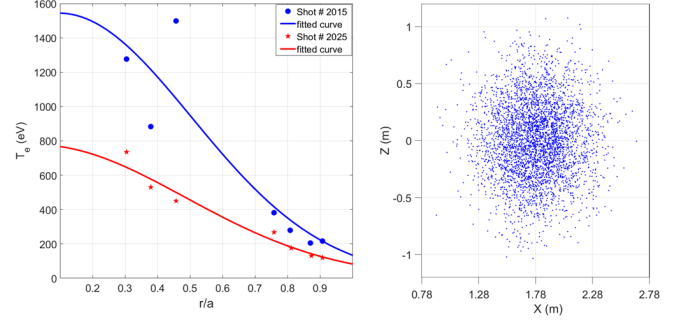


Fig. 8. (Color online) Left, the temperature data from HL-3 discharges (the blue dots and red stars are measured data, and blue curve and red curve are fitted profiles); right, the normal distribution of incident particles on the HL-3 plasma cross section in Geant4 simulations.

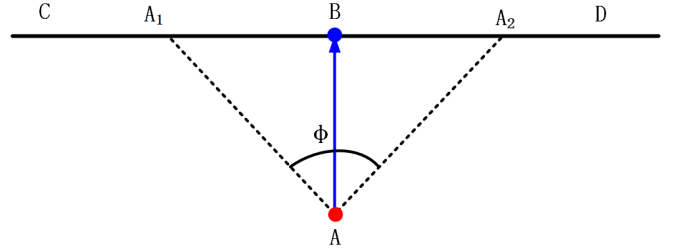


Fig. 9. (Color online) Schematic of fast-electron bremsstrahlung angle.

the X and Y directions, the distribution of particles in the Z direction can be defined by another set of random numbers with a normal distribution. Additionally, the particle moves along orbital AA' , and the probability of its appearance at any point in the orbit is random, which can be achieved by a random angle θ . Let

$$\theta = 2\pi\xi_A, \quad (3)$$

where ξ_A is a random number and $0 < \xi_A < 1$.

Two random numbers ξ_{s1} and ξ_{s2} can be used to obtain a pair of random variables that follow the standard normal distributions N_s and M_s , using the following formula:

$$\begin{aligned} M_s &= \sqrt{(2\ln\xi_{s1})} \cdot \cos(2\pi\xi_{s2}) \\ N_s &= \sqrt{(2\ln\xi_{s1})} \cdot \sin(2\pi\xi_{s2}) \end{aligned}, \quad (4)$$

where $0 < \xi_{s1}, \xi_{s2} < 1$.

According to previous descriptions, let

$$\begin{aligned} \delta_{s1} &= \delta_{s2} = M_s \\ \delta_{s3} &= N_s \end{aligned}, \quad (5)$$

such that the point set $\{\{X_0 + \delta_{s1}\}, \{Y_0 + \delta_{s2}\}, \{Z_0 + \delta_{s3}\}\}$ follows the standard normal distribution, and can be written as follows:

$$\begin{aligned}
X_S &= \sigma_{s1} \cdot \delta_{s1} + X_0 \\
&= (\sigma_{s1} \cdot \delta_{s1} + R) \cdot \cos(\theta) \\
&= (\sigma_{s1} \cdot \sqrt{(-2\ln\xi_{s1})} \cdot \cos(2\pi\xi_{s2}) + R) \cdot \cos(\theta) \\
Y_S &= \sigma_{s2} \cdot \delta_{s2} + Y_0 \\
&= (\sigma_{s2} \cdot \delta_{s2} + R) \cdot \sin(\theta) \\
&= (\sigma_{s2} \cdot \sqrt{(-2\ln\xi_{s1})} \cdot \cos(2\pi\xi_{s2}) + R) \cdot \sin(\theta)
\end{aligned} \tag{6}$$

$$\begin{aligned}
Z_S &= \sigma_{s3} \cdot \kappa \cdot \delta_{s3} + Z_0 \\
&= \sigma_{s3} \cdot \kappa \cdot \sqrt{(-2\ln\xi_{s1})} \cdot \sin(2\pi\xi_{s2}) + Z_0
\end{aligned}$$

where σ_{s1} , σ_{s2} , and σ_{s3} are the plasma shape parameters and κ is the elongation of the HL-3 tokamak. The particle-distribution function can be expressed as follows:

$$G = G(X_S, Y_S, Z_S). \tag{7}$$

The next step is to construct an emission vector for each particle. When the fast electron moves along the orbit (red line) to A, its direction of motion is \vec{AB} because the center of the electron motion is perpendicular to the Z axis; thus, $\vec{AB} \perp \vec{OZ}$. The radiation of fast electron A is strongest along the direction of \vec{AB} , and the probability of other directions follows the distribution function $F(u, v, w)$.

Assuming $|\vec{AB}| = 1$, the coordinate value of $B(X, Y, Z)$ can be written as follows:

$$\begin{aligned}
X &= X_0 - Y_0/R \\
Y &= Y_0 + X_0/R \\
Z &= Z_0
\end{aligned} \tag{8}$$

To simplify our simulation model, we add an auxiliary line CD to describe the process, where CD passes through point B and is parallel to OA , as shown in Fig. 7. Similar to the previous description of the particle-distribution model, if we add a set of small variables $\{\{\delta_{d1}\}, \{\delta_{d2}\}, \text{and}\{\delta_{d3}\}\}$ that follow the normal distribution to each direction of point B , and then project all the points onto the line of CD , we obtain a point set $\{\{X + \delta_{d1}\}, \{Y + \delta_{d2}\}, \{Z + \delta_{d3}\}\}$, which follows the normal distribution along the line of CD and is located in the region of A_1A_2 , as shown in Fig. 9, where the maximum emission angle is Φ . The relationship between the maximum emission angle and length of A_1A_2 is

$$\tan\left(\frac{\Phi}{2}\right) = \frac{|\vec{A_1A_2}|}{|\vec{AB}|}. \tag{9}$$

The emission angle is obtained by varying the lengths of A_1A_2 .

Point A is connected to each point on the set $\{\{X + \delta_{d1}\}, \{Y + \delta_{d2}\}, \{Z + \delta_{d3}\}\}$, and these lines are considered as the propagation direction of the X/γ -ray photons. Thus, we obtain a forward-scattering model for each electron.

Two random numbers ξ_{d1} and ξ_{d2} are used to obtain a pair of random variables M_d and N_d , which follow a standard normal distribution:

$$\begin{aligned}
M_d &= \sqrt{(2\ln\xi_{d1})} \cdot \cos(2\pi\xi_{d2}) \\
N_d &= \sqrt{(2\ln\xi_{d1})} \cdot \sin(2\pi\xi_{d2})
\end{aligned} \tag{10}$$

and then let

$$\begin{aligned}
\delta_{d1} &= \delta_{d2} = M_d \\
\delta_{d3} &= N_d
\end{aligned} \tag{11}$$

Point set $\{\{X + \delta_{d1}\}, \{Y + \delta_{d2}\}, \{Z + \delta_{d3}\}\}$ follows a standard normal distribution and can be written as follows:

$$\begin{aligned}
X_D &= X + (\sigma_{d1} \cdot \delta_{d1}) \cdot Y_0/R \\
&= X + \sqrt{(-2\ln\xi_{d1})} \cdot \cos(2\pi\xi_{d2}) \cdot Y_0/R \\
Y_D &= Y + (\sigma_{d2} \cdot \delta_{d2}) \cdot X_0/R \\
&= Y + \sqrt{(-2\ln\xi_{d1})} \cdot \cos(2\pi\xi_{d2}) \cdot X_0/R \\
Z_D &= Z + \sigma_{d3} \cdot \delta_{d3} \\
&= Z + \sqrt{(-2\ln\xi_{d1})} \cdot \sin(2\pi\xi_{d2})
\end{aligned} \tag{12}$$

where $0 < \xi_{d1}, \xi_{d2} < 1$ and $\sigma_{d1}, \sigma_{d2}, \sigma_{d3}$ are the emission-angle parameters. The emission vectors of each particle are

$$\begin{aligned}
u &= X_D - X_0 \\
&= \sqrt{(-2\ln\xi_{d1})} \cdot \cos(2\pi\xi_{d2}) \cdot Y_0/R \\
v &= Y_D - Y_0 \\
&= \sqrt{(-2\ln\xi_{d1})} \cdot \cos(2\pi\xi_{d2}) \cdot X_0/R \\
w &= Z_D - Z_0 \\
&= \sqrt{(-2\ln\xi_{d1})} \cdot \sin(2\pi\xi_{d2})
\end{aligned} \tag{13}$$

The emission-angle distribution function can be expressed as

$$F = F(u, v, w). \tag{14}$$

Because the cross section of the X-ray emission cone is circular, that is, symmetrical in the X, Y, and Z directions, we

obtain $\sigma_{d1} = \sigma_{d2} = \sigma_{d3}$. If the emission angle Φ is known, we can derive $\overrightarrow{A_1 A_2}$ from Eq. 9 and the values of σ_{d1} , σ_{d2} , and σ_{d3} .

In summary, the key to the construction of the fast-electron bremsstrahlung model is to determine the particle-distribution and radiation-direction models. The particle-distribution model $G(X_S, Y_S, Z_S)$ generates the location of each photon, and the radiation-direction model $F(u, v, w)$ indicates the direction in which the photons move.

IV. SIMULATION RESULTS

Geant4 traces each X/γ -ray photon until it is deposited on the target detector or lost from space, and the code records all particle-deposition locations and deposition energies on the detector. The output data format is listed in Tab. 1.

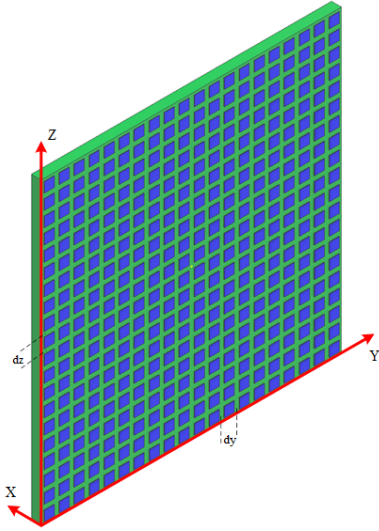


Fig. 10. (Color online) Simple schematic of the detector, where the blue squares are detector units, the X-, Y-, and Z-axes represent the thickness, width, and height of the detector, respectively, and dy and dz are the distance of every two adjacent detector units in the Y and Z directions.

TABLE 1. Data structure of Geant4 simulation outputs.

X	Y	Z	Deposition Energy
x_1	y_1	z_1	E_1
x_2	y_2	z_2	E_2
...
x_n	y_n	z_n	E_n

X , Y , and Z are the thickness, width, and height of the detector, respectively. (As shown in Fig. 10, each blue square is a detector pixel, and the distance between each pair of ad-

jacent detectors are d_y and d_z in the Y and Z directions, respectively.

Because the size of the deposition position of the individual ray photons is almost negligible, the resultant radiation image consists of independent discontinuous pulses. To reconstruct the radiation image, the detector must be separated into uniform intervals and the deposited energy in each interval must be integrated. The main part of the algorithm is as follows:

$$s(i, j) = \text{sum}(E(y > y_{min} + (i - 1) \times d_y \ \& \ y < y_{min} + i \times d_y \ \& \ z > z_{min} + (j - 1) \times d_z \ \& \ z < z_{min} + j \times d_z)) \quad (15)$$

where s is the deposited energy in each unit area, i and j represent the cyclic variables in the Y and Z directions, y_{min} and z_{min} represent the minimum values of Y and Z, respectively, and d_y and d_z are the step widths in the Y and Z directions, respectively.

A. Cases with Different Particle Numbers

We first consider the same size of the plasma cross section (plasma radius of 0.65 m) and gradually increase the number of incident photons. Let $\sigma_{s1} = \sigma_{s2} = \sigma_{s3} = 1/6$. We can obtain the particle distribution in the X, Y, and Z directions using the particle-distribution model from Eq. 6 as shown in (a), (b), and (c) in Fig. 11. The emission angle $\Phi = 150^\circ$ and length of $\overrightarrow{A_1 A_2}$ can be calculated using Eq. 9; therefore, we can obtain σ_{d1} , σ_{d2} , σ_{d3} and generate the direction distribution along CD from Eq. 12, as shown in Fig. 11(d). Fig. 12 provides a more intuitive distribution map of the particle distribution in the HL-3 tokamak, where the color represents the normalized particle density, with the warmer colors indicating denser particles and cooler colors indicating fewer particles. The outer dark grids represent the plasma boundaries.

The simulation results are shown in Fig. 13. In this figure, the color bar represents the normalized energy-deposition value: the warmer colors represent more energy deposition, and the cooler colors represent less energy deposition. (a), (b), (c), (d), (e), and (f) represent the incident photon numbers of 2×10^8 , 4×10^8 , 1×10^9 , 5×10^9 , 1×10^{10} , and 2×10^{10} , respectively. When the number of incident photons is small, the energy deposition is relatively dispersed, and no obvious distribution characteristics are observed. However, as the number of incident photons increases, the energy-deposition distribution gradually becomes concentrated in the middle area, similar to the particle distribution shown in Fig. 12.

B. Cases with Different Plasma Sizes

We consider different sizes of plasma cross sections, all with sufficient incident photons of 2×10^{10} and fixed emission angles of 150° . The particle-source size can be adjusted by changing the values of σ_{s1} , σ_{s2} , and σ_{s3} . Fig. 14 shows

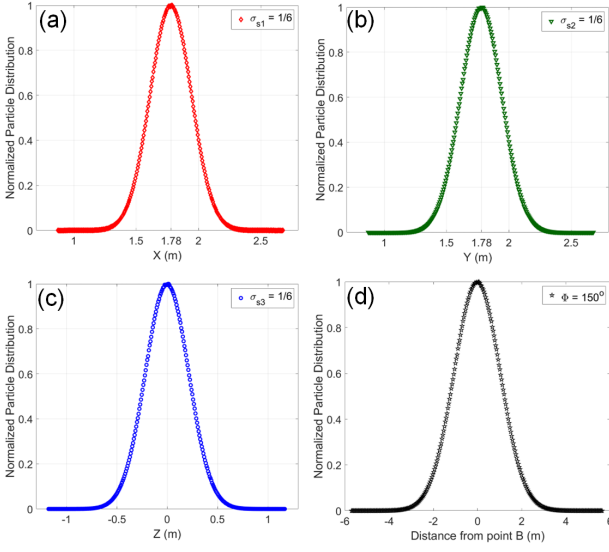


Fig. 11. (Color online) Normalized particle distribution (a) in the X direction, (b) in the Y direction, (c) in the Z direction, and (d) particle distribution around point B at $\Phi = 150^\circ$.

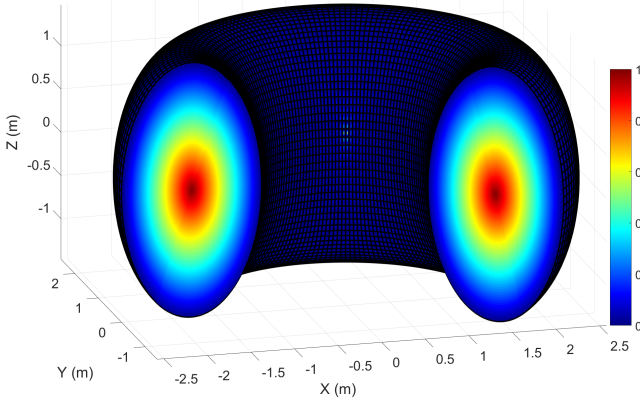


Fig. 12. (Color online) Normalized particle distribution on plasma cross-section, where the warmer colors indicate denser particles and cooler colors indicate fewer particles; the outer dark grids are plasma boundaries.

the cross section of the HL-3 tokamak and plasmas, in which (a), (b), (c), (d), (e), and (f) exhibit particle-source radii of 0.1 m, 0.2 m, 0.3 m, 0.4 m, 0.5 m, and 0.65 m (the maximum size of the HL-3 plasma), respectively, where the corresponding plasma-size parameters ($\sigma_{s1} = \sigma_{s2} = \sigma_{s3}$) are $1/40, 1/20, 1/10, 1/5, 1/2$, and $1/1$, respectively. The color in each figure represents the normalized particle distributions, where warmer colors indicate denser particles and cooler colors represent fewer particles.

Fig. 15 shows the simulation results. Even though the energy-deposition areas vary with different plasma cross-section sizes, all are symmetrically distributed. This suggests that the energy-deposition characteristics on the detectors are independent of the plasma size.

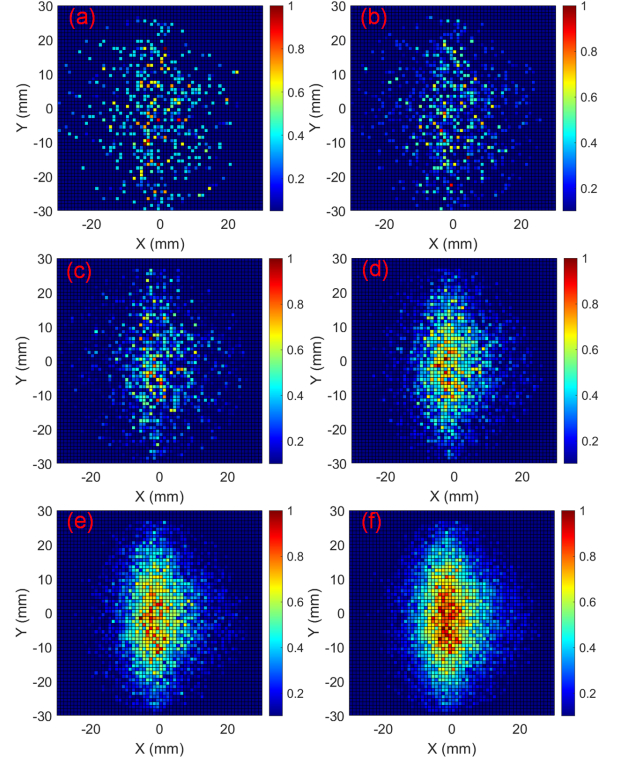


Fig. 13. (Color online) Normalized energy deposition on the detectors, where the warmer colors indicate higher energy deposition and cooler colors indicate lower energy deposition. (a) to (f) are incident photon numbers of $2 \times 10^8, 4 \times 10^8, 1 \times 10^9, 5 \times 10^9, 1 \times 10^{10}$, and 2×10^{10} , respectively.

C. Cases with Different Particle-Emission Angles

In HL-3 tokamak discharges, the energy of the ray photons generated by fast-electron bremsstrahlung is continuous. However, in our simulations, all initial photons are monoenergetic. According to the description in Section III, the cone angles of photon emissions generated by fast-electron bremsstrahlung with different energies are different; thus, we can use different cone angles to represent electrons with different energies.

The following formula assist in understanding this process:

$$E = k \cdot \frac{N}{V}, \quad (16)$$

where E is the total deposited energy of the incident photons on the detector, k is the energy of each photon, N is the total number of photons, and V is the space volume of the photon emission.

Because k is a constant value in our simulation, if the total incident photon number N is the same for each calculation, then the total energy E can be adjusted by changing the photon-emission volume V . Eq. 16 shows that the smaller the emission volume V , the larger the value of N/V , and the higher the energy deposition, and vice versa. The radiation model in Fig. 5 shows that the higher the electron energy, the narrower the bremsstrahlung cones, and as a result, the

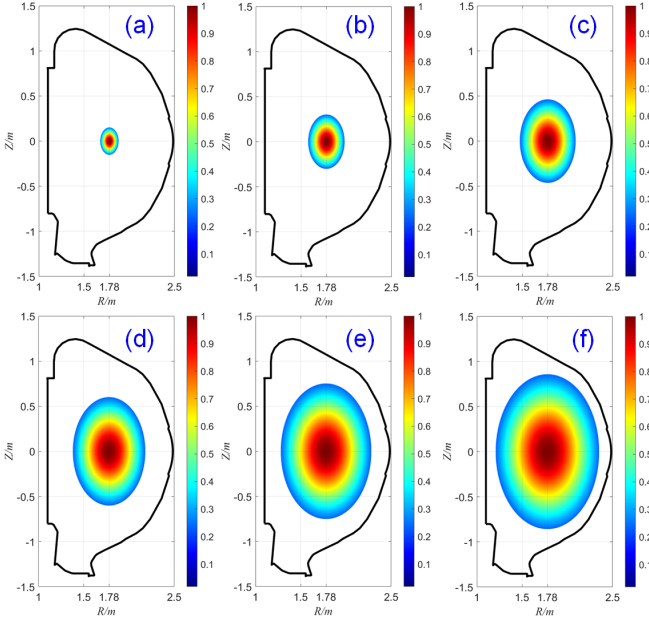


Fig. 14. (Color online) Normalized particle distribution on plasma cross section, where warmer colors indicate denser particles and cooler colors indicate fewer particles. (a) to (f) exhibit plasma cross sections with sizes of 0.1, 0.2, 0.3, 0.4, 0.5, and 0.65 m, respectively.

smaller the emission volume. Hence, the electron energies are related to the radiation-cone angles; a larger cone angle represents a smaller electron energy, whereas a smaller cone angle represents a larger electron energy.

In this subsection, we investigate the influence of the particle-radiation angle on energy deposition, all cases have sufficient incident photons of 2×10^{10} and a fixed plasma radius of $0.65m$. Fig. 16 exhibits four different radiation angles. To display all the angles in the same diagram, we divide the cone radius of the larger angle by the different coefficients. The red cone angle represents a radiation angle of 60° , twice the green cone radius represents a radiation angle of 120° , three times the blue cone radius represents a radiation angle of 150° , and six times the black cone radius represents a radiation angle of 170° .

Fig. 17 shows the simulation results under these radiation angles, (a), (b), (c), and (d) represent radiation angles of 60° , 120° , 150° , and 170° , respectively. The color bar in the figure represents the normalized energy-deposition value, where warmer colors represent more energy deposition and cooler colors indicate less energy deposition. A white elliptical dashed line is used to label the shape of the energy deposition. The diagram shows that when the radiation angle is small, the shape of the energy deposition tends to be circular, and when the radiation angle is large, the shape of the energy deposition becomes elliptical, and the aspect ratio of the ellipse increases with the angle. However, in all cases, the deposited energy is symmetrically distributed.

Although single-photon energy is used in our calculation, changing the radiation angle can represent different energy values to some extent. From the calculation results, changing

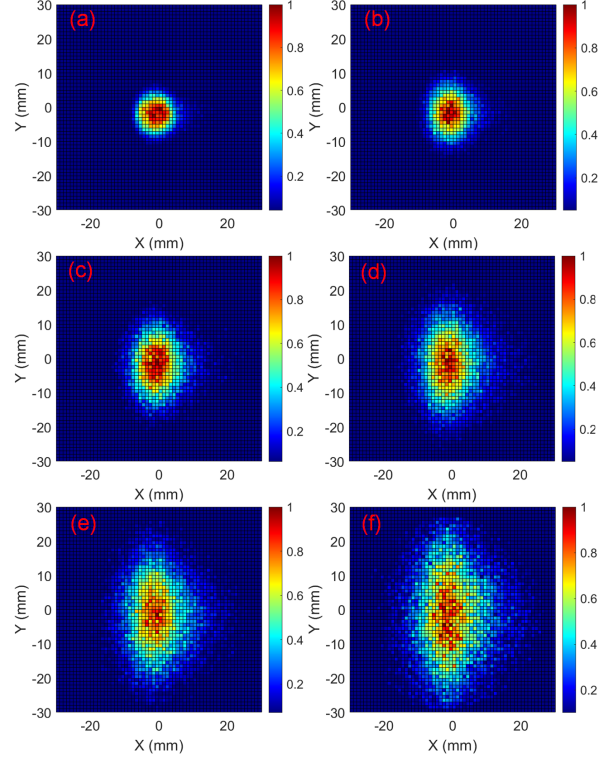


Fig. 15. (Color online) Normalized energy deposition on the detectors, where warmer colors exhibit higher energy deposition and cooler colors indicate lower energy deposition. (a) to (f) show cases of different plasma cross sections from Fig. 13.

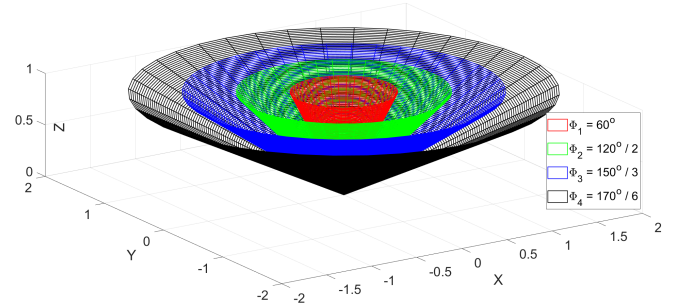


Fig. 16. (Color online) Fast-electron emission angles, where the red lines represent a maximum emission angle of 60° , the green lines represent a maximum emission angle of 120° , the blue lines represent a maximum emission angle of 150° , and the dark lines represent a maximum emission angle of 170° .

the radiation angle of the photons does not alter the symmetry distribution of the energy deposition. We believe that similar results can be obtained if the energy of the particle and its associated radiation angle are used as variables.

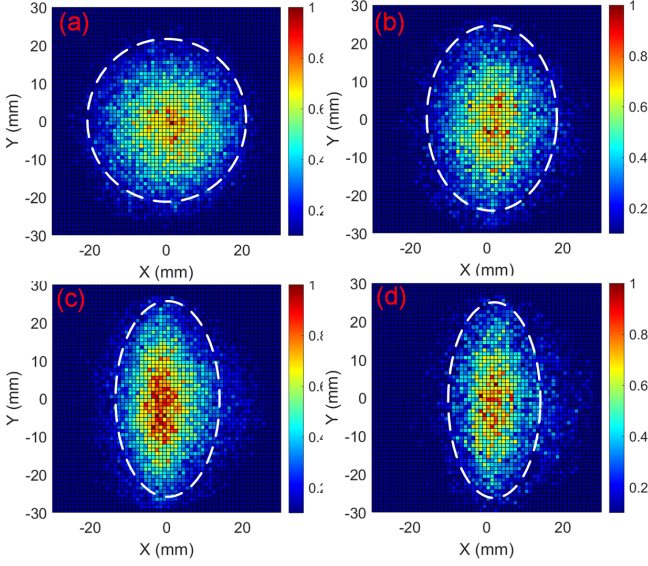


Fig. 17. (Color online) Normalized energy deposition on the detectors, where the warmer color represent higher energy deposition and cooler colors indicate lower energy deposition. (a) to (d) show cases of different emission angles from Fig. 16.

V. ANALYSIS MODEL OF ENERGY DEPOSITION ON THE DETECTOR

A 2D analytical model is developed to further explain the energy deposition that appears on the detector. Two main reasons exist for the symmetrical distribution of the deposited energy on the detector: the first is the forward-scattering effect of bremsstrahlung, and the second is the pinhole imaging effect. Owing to the symmetry in the Z direction, we consider only the middle plane of the HL-3 plasma. In Fig. 18, the red region is the midplane plasma, the black arcs are the plasma boundaries, and the green rectangle on the left is the location of the HXR-imaging system.

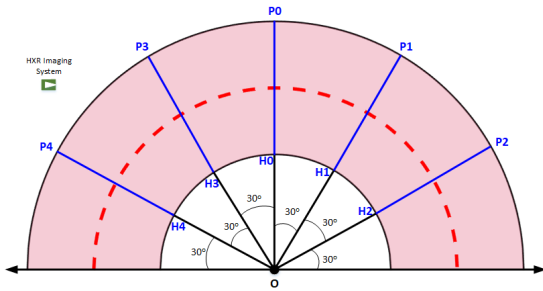


Fig. 18. (Color online) Middle plane of HL-3 plasma (red shadow), where the red dashed line is the magnetic axis and the left green box is the HXR-imaging system.

Energy deposition on the detector from a 2D plasma plane can be calculated by separating the plasma surface into multiple lines. For convenience of calculation, we list only a few

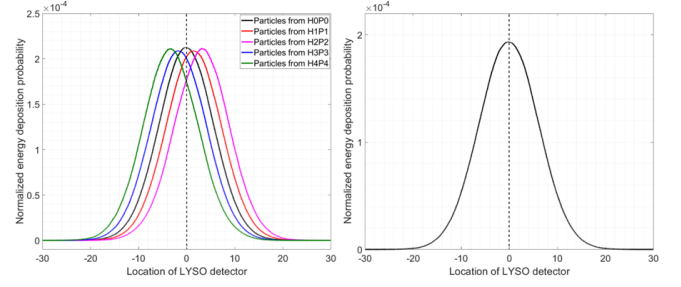


Fig. 19. (Color online) Normalized energy-deposition probability on the detector. Left, particles from H0P0, H1P1, H2P2, H3P3, and H4P4; right, average energy-deposition probability from these five lines.

lines, as shown in Fig. 18 with H0P0, H1P1, H2P2, H3P3, and H4P4; all the lines pass through the center point, and the angle between each pair of adjacent lines is 30° . The number of particles between H^* and P^* in each line follows a Gaussian distribution (consistent with the radial distribution of the electron temperature or density).

As introduced in Sec. III B, the probability of the photons emitted by an electron bremsstrahlung follows a Gaussian distribution centered on its direction of motion. The collimation pinhole in an HXR-imaging system is small and regarded as a point. Based on the principle of pinhole imaging, only photons in the direction of the connecting line between the positions of the electron and pinhole can reach the detector. If we record the deposited energy and location of each photon and add them, we obtain the energy distribution on the detector. Taking the i -th electron as an example, the position of the energy deposition can be calculated using a triangular relationship, and the energy value of the deposition can be calculated using the following equation:

$$E_i = E_p \times p_{di} \times p_{ei}, \quad (17)$$

where E_i is the normalized energy, E_p is the energy of a single photon, p_{di} is the normalized probability of electrons appearing at that position, and p_{ei} is the normalized probability of a photon passing through the pinhole.

Because the particle source is linear, the energy deposited on the detector is also linear. The calculated results are shown in Fig. 19. The deposited energy of photons emitted by electrons on the H0P0 line on the detector is symmetrically distributed about the middle line (the black curve in the left figure), whereas the deposited energy from other lines deviates from the middle line (the green, blue, red, and purple lines in the left figure). However, as shown in the diagram, the deposited energy from H1P1 and H3P3 are symmetrically distributed about the middle line, which is the same energy-distribution characteristic from lines H2P2 and H4P4. Adding the calculation results from all lines shows that the total deposited energy on the detector is still symmetrically distributed (the right figure).

Although our analytical model is 2D, we believe that if we consider the entire plasma range, a symmetric distribution of energy deposition still exists.

VI. SUMMARY AND DISCUSSION

A fast-electron bremsstrahlung imaging model is developed using the Monte Carlo simulation software Geant4, which is based on the plasma geometry and HXR-imaging system at the HL-3 tokamak. The distribution of fast electrons refers to the temperature and density during the RF wave current-drive experiments, and the forward scattering of fast-electron bremsstrahlung radiation is considered. Preliminary simulation results show that the energy deposition on the detector is symmetrically distributed as long as the number of particles is sufficiently large, even if the toroidal effect causes an asymmetrical plasma distribution. The deposited energy on the detector appears to have a distribution similar to that of the electron temperatures or densities of the plasma cross section during the RF-wave experiments. Multiple simulation results confirmed that the symmetric distribution characteristics remained when the particle-distribution model or fast-electron bremsstrahlung angle was changed.

Two-dimensional HXR-imaging systems are particularly important for the study of fast-electron physics; however, the spatial asymmetry of plasma poses some difficulties in analyzing experimental data. The simulation results compensated for this deficiency by constructing a relationship between the energy deposition on the detector and spatial distribution of the plasma parameters, indicating that the diagnostic data from the 2D imaging system can be directly used to analyze the 2D spatiotemporal evolution properties of fast electrons. Moreover, if the energy deposition on the detector is known, we can deduce the spatial-distribution characteristics of fast electrons or the fast-electron forward-scattering properties.

For future fusion-reactor-scale devices, the higher the plasma parameters, the greater is the role of fast electrons in maintaining the steady-state operation of the system. Ac-

curate measurement of the RF-wave power-deposition location is important for optimizing RF-wave heating and current drive. Moreover, high time-space-resolved fast-electron radiation evolution is the most direct and effective method to study plasma disruptions and fast-electron-driven unstable modes. The simulation results can both optimize the design of the diagnostic system and assist in the analysis of the experimental data obtained from the imaging system. Thus, the physical problems related to fast electrons can be analyzed in greater depth.

However, in all the calculations, desirable distribution images can only be obtained when the number of particles is sufficiently large. Energy deposition on the detector is highly dependent on the particle-source distribution and emission angle of the fast-electron forward-scattering radiation. However, it limits the temporal resolution of the imaging system, and longer measurement times are needed to obtain clearer energy-deposition results. However, this also limits the range of use of imaging systems. Under low-plasma parameter discharges, the number of X-ray photons produced per unit time is low, which is not conducive to the analysis of the results.

As mentioned in the Introduction, the application of auxiliary heating methods, disruption events, and sawtooth activities can produce a large number of fast electrons and X/γ - ray photons per unit time, which provides favorable conditions for improving the measurement accuracy and temporal resolution of the HXR-imaging system. Therefore, this diagnostic system has excellent application prospects.

Because the radiation angle is related to the energy of fast electrons, we will update our particle-distribution and emission-angle models by considering the energy distribution of fast electrons in the HL-3 RFW plasma in future work. The computational model will be optimized based on diagnostic data from the HXR-imaging system, and an energy-spectrum algorithm program will be developed in the near future.

-
- [1] A. Lazaros, A model for the interaction of superthermal electrons with the magnetohydrodynamic modes during electron cyclotron resonant heating. *Phys. Plasmas*. **6**, 148-152 (1999). <https://doi.org/10.1063/1.873269>
 - [2] A. Lazaros, Development of a superthermal electron avalanche and tearing mode suppression during electron cyclotron resonant heating. *Phys. Plasmas*. **8**, 1263-1266 (2001). <https://doi.org/10.1063/1.1355028>
 - [3] T. Kunugi, Effects of runaway electrons on plasma facing component. *Fusion Eng. Des.* **23**, 329-339 (1994). [https://doi.org/10.1016/0920-3796\(94\)90017-5](https://doi.org/10.1016/0920-3796(94)90017-5)
 - [4] V. Riccardo, P. Andrew, L. C. Ingesson et al., Disruption heat loads on the JET MkIIIGB divertor. *Plasma Phys. Controlled Fusion*. **44**, 905 (2002). <https://doi.org/10.1088/0741-3335/44/6/319>
 - [5] B. Bazylev, G. Arnoux, S. Brezinsek et al., Modeling of the impact of runaway electrons on the ILW in JET. *J. Nucl. Mater.* **438**, S237-S240 (2013). <https://doi.org/10.1016/j.jnucmat.2013.01.035>
 - [6] G. F. Matthews, B. Bazylev, A Baron-Wiechec et al., Melt damage to the JET ITER-like Wall and divertor. *Phys. Scr.* **T167**, 014070 (2016). <https://doi.org/10.1088/0031-8949/T167/1/014070>
 - [7] Z. Wang, Q. H. Huang, Q. Y. Tan et al., The effect of heat load on divertor target by pumping in HL-2A Tokamak. *Nucl. Tech.* **45**, 100603 (2022). <https://doi.org/10.11889/j.0253-3219.2022.hjs.45.100603>(in Chinese)
 - [8] S. Gnesin, S. Coda, J. Decker et al., Suprathermal electron studies in the TCV tokamak: Design of a tomographic hard-X-ray spectrometers. *Rev. Sci. Instrum.* **79**, 10F504 (2008). <https://doi.org/10.1063/1.2957843>
 - [9] M. Brusati, D. V. Bartlett, A. Ekedahl et al., Determination of the suprathermal electron distribution function during lower hybrid current drive in JET. *Nucl. Fusion*. **34**, 23 (1994). <https://doi.org/10.1088/0029-5515/34/1/I02>
 - [10] Z. M. Wang, L. Z. Li, The measurements of hard X-ray fluctuations in the HT-6B Tokamak. *Acta. Physica Sinica*. **36**, 960-964 (1987). <https://doi.org/10.7498/aps.36.960>(in Chinese)
 - [11] Y. J. Shi, B. L. Ling, B. N. Wan et al., A Study on hard X-ray radiation during lower hybrid current drive on HT-7 superconducting tokamak. *Nucl. Tech.* **12**, 846-850 (2000)(Chinese).
 - [12] S. Y. Lin, Y. J. Shi, B. N. Wan et al., Hard X-ray PHA system

- on the HT-7 tokamak. *Plasma Sci Technol.* **8**, 261–264 (2006). <https://doi.org/10.1088/1009-0630/8/3/03>
- [13] Y. Xi, S. Y. Lin, L. Q. Hu et al., Measurement 20–200 keV hard X-ray based on CdTe detector in EAST Tokamak. *Nucl. Tech.* **36**, 020203 (2013). <https://doi.org/10.11889/j.0253-3219.2013.hjs.36.020203>(in Chinese)
- [14] J. W. Yang, G. Y. Zhang, C. X. Zeng et al., Measurement and Study of Hard X-ray Bremsstrahlung emission with LHCD in the HL-1M Tokamak. *Nucl. Fusion Plasma Phys.* **17**, 28–33 (1997). <https://doi.org/10.16568/j.0254-6086.1997.03.006>(in Chinese)
- [15] Y. F. Zhao, W. W. Fan, C. Yuan et al., Study of a new type of hard X-ray detector for HL-2A device. *Nucl. Tech.* **40**, 040402 (2017). <https://doi.org/10.11889/j.0253-3219.2017.hjs.40.040402> (in Chinese)
- [16] W. W. Fan, B. W. Zheng, J. Cao et al., Development of a fast electron bremsstrahlung diagnostic system based on LYSO and silicon photomultipliers during lower hybrid current drive for tokamak. *Plasma Sci. Technol.* **21**, 65104–065104 (2019). <https://doi.org/10.1088/2058-6272/ab0a77>
- [17] S. K. Cheng, Y. B. Zhu, Z. Y. Chen et al., Tangential hard x-ray diagnostic array on EXL-50 spherical tokamak. *Rev. Sci. Instrum.* **92**, 043513 (2021). <https://doi.org/10.1063/5.0040636>
- [18] D. Choi, A. Merle, S. Coda et al., Suprathermal electron driven fishbone instability in the TCV tokamak. *Plasma Phys. Controlled Fusion.* **62**, 025006 (2019). <https://doi.org/10.1088/1361-6587/ab5147>
- [19] T. Barbui, O. Chellai, L. F. Delgado-Aparicio et al., Design and engineering challenges of a multi-energy hard X-ray camera for long-pulse profile measurements at WEST tokamak. *Fusion Eng. Des.* **173**, 112957 (2021). <https://doi.org/10.1016/j.fusengdes.2021.112957>
- [20] Y. P. Zhang, D. Mazon, Y. Peysson et al., Measurements of the fast electron bremsstrahlung during lower hybrid current drive in the HL-2A tokamak. *AIP Adv.* **9**, 085019 (2019). <https://doi.org/10.1063/1.5110233>
- [21] Y. P. Zhang, D. Mazon, J. Zhang et al., A Hard X-Ray Pin-hole Camera System for Fast Electron Bremsstrahlung Measurements in the HL-2A Tokamak. *Fusion Sci. Technol.* **77**, 1–8 (2021). <https://doi.org/10.1080/15361055.2020.1829457>
- [22] D. W. Huang, Z. Y. Chen, Y. H. Luo et al., Hard X-ray spatial array diagnostics on Joint Texas Experimental Tokamaka. *Rev. Sci. Instrum.* **85**, 11D845 (2014). <https://doi.org/10.1063/1.4891709>
- [23] P. V. Savrukhn, A. I. Ermolaeva, E. A. Shestakov et al., Tomographic analysis of the nonthermal X-ray bursts during disruption instability in the T-10 tokamak. *Rev. Sci. Instrum.* **85**, 103508 (2014). <https://doi.org/10.1063/1.4898333>
- [24] Y. Peysson, F. Imbeaux, Tomography of the fast electron bremsstrahlung emission during lower hybrid current drive on TORE SUPRA. *Rev. Sci. Instrum.* **70**, 3987–4007 (1999). <https://doi.org/10.1063/1.1150025>
- [25] M. Anton, H. Weisen, M. J. Dutch et al., X-ray tomography on the TCV tokamak. *Plasma Phys. Controlled Fusion.* **38**, 1849 (1996). <https://doi.org/10.1088/0741-3335/38/11/001>
- [26] R. Kaita, S. V. Goeler, S. Sesnic et al., Two-dimensional hard x-ray imaging diagnostic for lower hybrid current drive experiments in PBX-M. *Rev. Sci. Instrum.* **61**, 2756–2758 (1990). <https://doi.org/10.1063/1.1141821>
- [27] S. V. Goeler, S. Jones, R. Kaita et al., Camera for imaging hard x rays from suprathermal electrons during lower hybrid current drive on PBX-M. *Rev. Sci. Instrum.* **65**, 1621–1630 (1994). <https://doi.org/10.1063/1.1144850>
- [28] S. V. Goeler, H. Fishman, D. Ignat et al., The simulation of hard x-ray images obtained during lower hybrid current drive on the Princeton Beta Experiment Modification. *Phys. Plasmas.* **2**, 205–217 (1995). <https://doi.org/10.1063/1.871092>
- [29] S. E. Jones, S. V. Goeler, S. Bernabei et al., Calculation of an upper limit for an effective fast electron diffusion constant using the hard X-ray camera on PBX-M. *Plasma Phys. Controlled Fusion.* **35**, 1003 (1993). <https://doi.org/10.1088/0741-3335/35/8/008>
- [30] S. E. Jones, J. Kesner, S. Luckhardt et al., Fast electron transport and lower hybrid absorbed power profiles from hard x-ray imaging in the Princeton Beta Experiment-Modified. *Phys. Plasmas.* **2**, 1548–1560 (1995). <https://doi.org/10.1063/1.871484>
- [31] D. C. Pace, C. M. Cooper, D. Taussig et al., Gamma ray imager on the DIII-D tokamak. *Rev. Sci. Instrum.* **87**, 043507 (2016). <https://doi.org/10.1063/1.4945566>
- [32] C. M. Cooper, D. C. Pace, C. Paz-Soldan et al., Applying the new gamma ray imager diagnostic to measurements of runaway electron Bremsstrahlung radiation in the DIII-D Tokamak (invited). *Rev. Sci. Instrum.* **87**, 11E602 (2016). <https://doi.org/10.1063/1.4961288>
- [33] A. Lvovskiy, C. Paz-Soldan, N. Eidiets et al., Upgrades to the gamma ray imager on DIII-D enabling access to high flux hard X-ray measurements during the runaway electron plateau phase (invited). *Rev. Sci. Instrum.* **93**, 113524 (2022). <https://doi.org/10.1063/5.0101690>
- [34] A. D. Molin, L. Fumagalli, M. Nocente et al., Novel compact hard X-ray spectrometer with MCps counting rate capabilities for runaway electron measurements on DIII-D. *Rev. Sci. Instrum.* **92**, 043517 (2021). <https://doi.org/10.1063/5.0043762>
- [35] Q. Li, The component development status of HL-2M tokamak. *Fusion Eng. Des.* **96–97**, 338–342 (2015). <https://doi.org/10.1016/j.fusengdes.2015.06.106>
- [36] X. R. Duan, M. Xu, W. L. Zhong et al., Progress of HL-2A experiments and HL-2M program. *Nucl. Fusion.* **62**, 042020 (2022). <https://doi.org/10.1088/1741-4326/ac3be6>
- [37] X. Song, X. M. Song, B. Li et al., Plasma initiation and preliminary magnetic control in the HL-2M tokamak. *Nucl. Fusion.* **61**, 086010 (2021). <https://doi.org/10.1088/1741-4326/ac09fc>
- [38] J. Cao, C. Y. Jiang, Y. F. Zhao et al., A novel compact Tokamak Hard X-ray diagnostic detector. *Nucl. Sci. Tech.* **26**, 060402 (2015). <https://doi.org/10.13538/j.1001-8042/nst.26.060402>
- [39] W. K. Chen, L. Q. Hu, G. Q. Zhong et al., Optimization study and design of scintillating fiber detector for D-T neutron measurements on EAST with Geant4. *Nucl. Sci. Tech.* **33**, 139 (2022). <https://doi.org/10.1007/s41365-022-01123-w>
- [40] W. K. Chen, L. Q. Hu, G. Q. Zhong et al., Study on the gamma rays and neutrons energy response optimization of a scintillating fiber detector for EAST with Geant4. *Nucl. Sci. Tech.* **34**, 134 (2023). <https://doi.org/10.1007/s41365-023-01290-4>
- [41] S. K. Cheng, Y. P. Zhang, H. B. Xu et al., Tangentially viewing hard X-ray imaging system and its measurement simulation on the HL-2M tokamak. *Fusion Eng. Des.* **193**, 113798 (2023). <https://doi.org/10.1016/j.fusengdes.2023.113798>
- [42] S. Agostinelli, J. Allison, K. Amako et al., Geant4—a simulation toolkit. *Nucl. Instrum. Methods Phys. Res., Sect. A.* **506**, 250–303 (2003). [https://doi.org/10.1016/S0168-9002\(03\)01368-8](https://doi.org/10.1016/S0168-9002(03)01368-8)
- [43] J. Allison, K. Amako, J. Apostolakis et al., Geant4 developments and applications. *IEEE Trans. Nucl. Sci.* **53**, 270–278 (2006). <https://doi.org/10.1109/TNS.2006.869826>
- [44] S. V. Goeler, J. Stevens, S. Bernabei et al., Angular dis-

tribution of the bremsstrahlung emission during lower hy-

brid current drive on PLT. Nucl. Fusion. **25**, 1515 (1985).
<https://doi.org/10.1088/0029-5515/25/11/001>